

Energy & Environmental Science

Accepted Manuscript



This is an *Accepted Manuscript*, which has been through the Royal Society of Chemistry peer review process and has been accepted for publication.

Accepted Manuscripts are published online shortly after acceptance, before technical editing, formatting and proof reading. Using this free service, authors can make their results available to the community, in citable form, before we publish the edited article. We will replace this *Accepted Manuscript* with the edited and formatted *Advance Article* as soon as it is available.

You can find more information about *Accepted Manuscripts* in the [Information for Authors](#).

Please note that technical editing may introduce minor changes to the text and/or graphics, which may alter content. The journal's standard [Terms & Conditions](#) and the [Ethical guidelines](#) still apply. In no event shall the Royal Society of Chemistry be held responsible for any errors or omissions in this *Accepted Manuscript* or any consequences arising from the use of any information it contains.

Lead-Free Organic-Inorganic Tin Halide Perovskites for Photovoltaic Applications

Cite this: DOI: 10.1039/x0xx00000x

Nakita K. Noel,^a Samuel D. Stranks,^a Antonio Abate,^a Christian Wehrenfennig,^a Simone Guarnera,^{b,c} Amir Abbas Haghighirad,^a Aditya Sadhanala,^d Giles E. Eperon,^a Michael B. Johnston,^a Anna Maria Petrozza,^b Laura M. Herz,^a Henry J. Snaith^{a*}

Received 00th January 2012,
Accepted 00th January 2012

DOI: 10.1039/x0xx00000x

www.rsc.org/

Already exhibiting solar to electrical power conversion efficiencies of over 16 %, organic-inorganic lead halide perovskite solar cells are one of the most promising emerging contenders in the drive to provide a cheap and clean source of energy. One concern however, is the potential toxicology issue of lead, a key component in the archetypical material. The most likely substitute is tin, which like lead, is also a group 14 metal. While organic-inorganic tin halide perovskites have shown good semiconducting behaviour, the instability of tin in its 2+ oxidation state has thus far proved to be an overwhelming challenge. Here we report the first completely lead-free, CH₃NH₃SnI₃ perovskite solar cell processed on a mesoporous TiO₂ scaffold, reaching efficiencies of over 6% under 1 sun illumination. Remarkably, we achieve open circuit voltages over 0.88 V from a material which has a 1.23 eV band gap.

1. Introduction

With increasing industrialisation and a growing population, the energy demands of today's society will continue to grow. Faced with a dwindling supply of fossil fuels and adverse climate change, the search for a viable source of renewable energy is ongoing. Of all available forms of renewable energy, solar energy is one of the most promising. At present, the photovoltaic market is dominated by solar cells made of crystalline silicon however, even in light of the major decrease in the price of crystalline silicon, the high production and installation costs lead to long payback times in most regions, decreasing the economic feasibility of widespread use.¹

As such, there has been a concerted effort to find a cheaper alternative to silicon solar cells. Recently, perovskite-based solar cells have been developed and have rapidly passed the efficiencies of many emerging and commercial photovoltaics, such as dye-sensitised,² organic and amorphous silicon solar cells.³ The term perovskite is given to all compounds which have the general chemical formula ABX₃, and the crystal structure of calcium titanate (CaTiO₃). Organic-inorganic metal trihalide perovskites (where A is an organic cation, B a divalent metal ion, and X a halide or any mixture thereof) such as CH₃NH₃PbX₃, are promising alternatives to silicon, having both cheap and abundant starting materials, and being able to be manufactured by simple solution processing^{4,6} or scalable vapour phase deposition methods.^{7,8} The first report of a solar

cell incorporating a perovskite absorber was by Miyasaka and co-workers in 2009 and showed a 3.8% efficient perovskite sensitised solar cell employing a liquid electrolyte.⁹ This efficiency was further increased to 6.5% by Park et al. in 2011.¹⁰ However, due to the corrosive nature of the liquid electrolyte, the perovskite material was dissolved within a few minutes of device operation. This prompted a shift towards solid-state hole conductors and within the last two years alone, the efficiencies of perovskite solar cells have leapt from around 10%^{4,5,11} to a certified 16.2% (NREL).¹²

One concern with this material is the toxicity of lead, and as such, a key scientific challenge is to replace the lead in the perovskite crystal with a less toxic metal, but no successes have yet been reported. The most viable replacements for Pb in the perovskite material are Sn and Ge, also members of the group 14 metals. However, it is well known that the stability of the 2+ oxidation state decreases when moving up the group 14 elements, thus the major problem with the use of these metals is their chemical instability in the required oxidation state. Sn-based perovskites in particular, have shown excellent mobilities in transistors,¹³ but can also be intentionally or unintentionally doped to become metallic.^{14,15} It has been demonstrated that when the Sn²⁺ ion is oxidised to Sn⁴⁺, the Sn⁴⁺ acts as a p-type dopant within the material in a process referred to as "self-doping".¹⁴ To the best of our knowledge, there exists no previous report of a solar cell utilising a completely Pb-free, Sn-based perovskite as the absorber layer. A recent study by

Ogimi *et al.* reported a mixed metal, Sn-Pb perovskite which allowed tunability of the band gap of the perovskite absorber by varying the Sn:Pb ratio, indicating that Sn could be a good choice of metal ion, especially for lower band gap solar cells.¹⁶ However, the same study reported that the neat $\text{CH}_3\text{NH}_3\text{SnI}_3$ perovskite does not exhibit significant photovoltaic properties, and that a minimum content of Pb is needed to stabilize Sn in its 2+ oxidation state.

Here we present materials and solar cell characterisation of photovoltaic devices employing the completely lead-free perovskite, methylammonium tin triiodide ($\text{CH}_3\text{NH}_3\text{SnI}_3$) as the photoactive material. Encapsulation of this material under inert atmosphere has allowed us to characterise the films and probe their performance in solar cells. We have obtained devices which yield power conversion efficiencies of greater than 6% under simulated full sunlight. We additionally derive the THz mobility and charge-carrier lifetime, which indicate that with reduction of the hole-doping density and further optimisation, this material should prove to be a viable, completely non-toxic alternative to Pb-based perovskite solar cells, with the potential to deliver even higher efficiencies. Importantly, this demonstrates that Pb-based materials are not unique in delivering efficient perovskite solar cells.

2. Results and discussion

Due to the instability of $\text{CH}_3\text{NH}_3\text{SnX}_3$ (where X= Cl, Br, I) in ambient atmosphere, we carried out all material and device processing in a nitrogen filled glovebox. We dissolved equimolar quantities of SnI_2 and $\text{CH}_3\text{NH}_3\text{I}$ in degassed N-dimethylformamide (DMF), and then spin-coated the solution onto the desired substrates (fluorine doped tin oxide (FTO) coated in compact TiO_2 and mesoporous TiO_2 or Al_2O_3 ,^{5, 17} for devices, Al_2O_3 or TiO_2 coated glass for photoluminescence measurements, and Al_2O_3 or TiO_2 coated z-cut quartz for terahertz spectroscopy samples) at 2000 rpm for 45 seconds. The dark brown, $\text{CH}_3\text{NH}_3\text{SnI}_3$ perovskite (**Figure S1**) was formed on the substrate during spin-coating and required no further heating to crystallise. If after formation, the film was taken out into ambient atmosphere, we observed a decolouration of the film which occurred within seconds, suggesting a rapid degradation of the material. The instability of this material in ambient conditions is likely to be derived from the inherent instability of the Sn^{2+} ion in the presence of oxygen and moisture.

Under ambient conditions, the Sn^{2+} ion will rapidly oxidise to its more stable Sn^{4+} analogue. This process will destroy the charge neutrality of the perovskite structure and cause it to break down, resulting in the formation of oxides/hydroxides of Sn and methylammonium iodide (MAI). The diffraction pattern of an air-exposed sample of $\text{CH}_3\text{NH}_3\text{SnI}_3$ is shown in the supplementary information (See **Figure S2**). In light of this, all measurements on this material were carried out on samples which were prepared and sealed under inert atmosphere. The exceptions to this were the samples prepared for scanning electron microscopy (SEM) and terahertz spectroscopy which remained unsealed, since the imaging and measurements were carried out under vacuum.

In order to investigate the structure and purity of the material, we performed X-ray diffraction (XRD) measurements. The diffraction pattern obtained (see **Figure 1**) is in good agreement with simulated and literature data, and corresponds to the tetragonal conformation of the perovskite structure.¹⁸ The

structure is identical to that of the more widely used $\text{CH}_3\text{NH}_3\text{PbX}_3$ perovskite,^{5, 17} showing that in this case, changing the central metal atom has not affected the overall crystal structure of the material. The lattice parameters derived from the X-Ray diffractogram were $a = 8.7912 \text{ \AA}$ and $c = 4.4770 \text{ \AA}$.

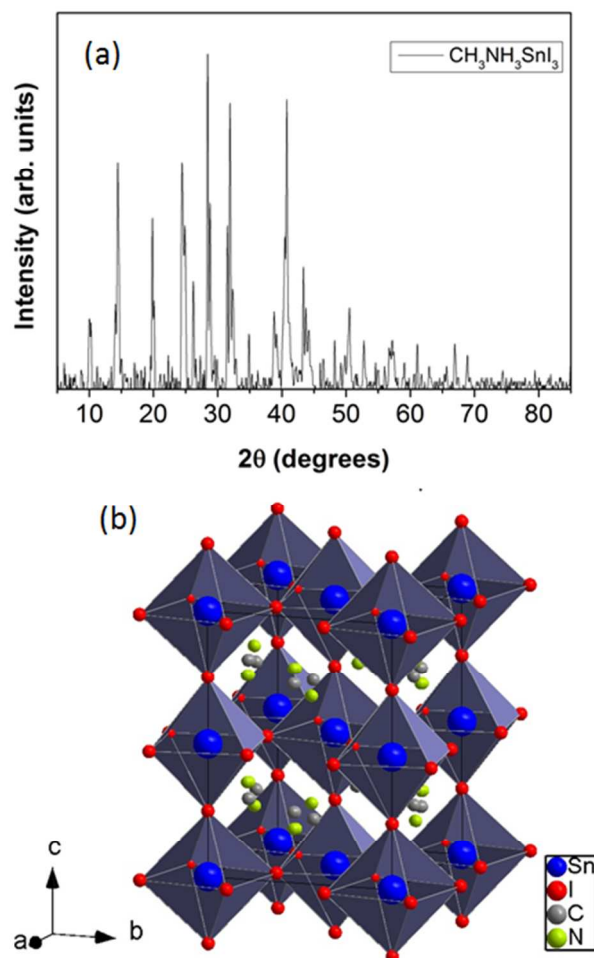


Figure 1: X-ray Diffraction (XRD) and Crystal Structure. (a) XRD pattern derived from a ground powder of $\text{CH}_3\text{NH}_3\text{SnI}_3$. (b) Simulated crystal structure of $\text{CH}_3\text{NH}_3\text{SnI}_3$ obtained from the diffraction pattern given in (a) showing the tetragonal conformation of the perovskite lattice.

The optical characterization of the material is shown in **Figure 2a**. The optical absorption characteristics of the material show a broad absorption edge at approximately 1000 nm and a broad photoluminescence peak at 980 nm. In comparison, the lead perovskite, $\text{CH}_3\text{NH}_3\text{PbI}_{3-x}\text{Cl}_x$, shows a sharper absorption edge at 770 nm, and a narrower emission spectrum which has been recently shown to be homogeneously broadened.¹⁹ In order to provide a good estimation of the band gap of the $\text{CH}_3\text{NH}_3\text{SnI}_3$ perovskite, we employed photo-thermal deflection spectroscopy (PDS).²⁰ In **Figure 2b** we show the absorption profile extracted from the PDS measurements. The Tauc plot shown in the inset shows a sharp band edge at 1.23 eV.

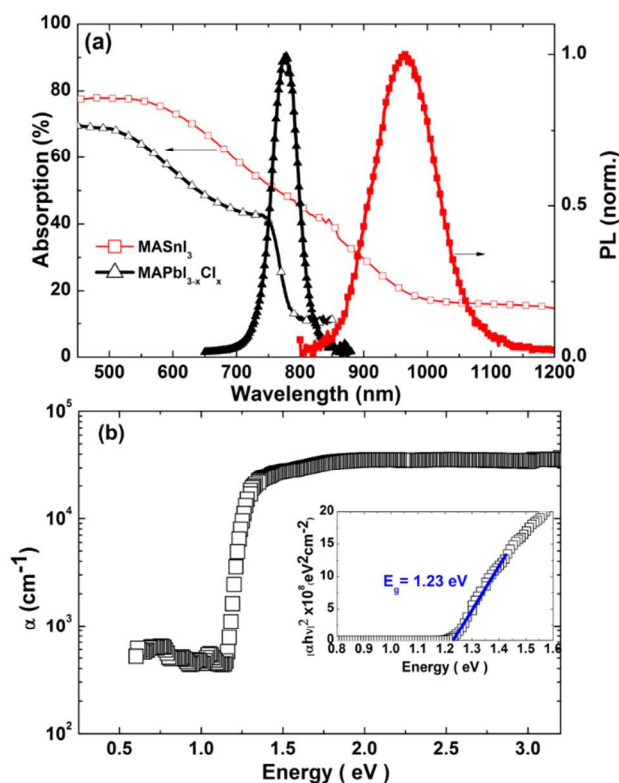


Figure 2: (a) Normalized steady state photoluminescence (PL) with photoexcitation at 500 nm, and absorption taken with reflectance and transmission employing an integrating sphere of the tin-based and lead-based perovskites CH₃NH₃SnI₃ and CH₃NH₃PbI_{3-x}Cl_x respectively. (b) The absorption profile of CH₃NH₃SnI₃ as determined through photo-thermal deflection spectroscopy (PDS), with the band gap of the material determined using the Tauc plot (shown in inset).²¹ We note that since there may be strong exciton absorption at the band edge, the Tauc plot determined band gap can only be considered as an estimate.

Unlike the Pb-based perovskite which requires heating to crystallise, the Sn perovskites crystallise at room temperature. This is actually an impediment to uniform film formation, as has previously been observed for MAPbBr₃ which also crystallises directly upon spin-coating.^{9, 22} Directly upon spin coating, the CH₃NH₃SnI₃ film crystallises, and in the case of a thin mesoporous TiO₂ layer, large crystalline platelets can form on top of the surface in addition to the material which penetrates the pores. These crystalline platelets are apparent in the scanning electron microscopy (SEM) images shown in **Figure 3a**. This image displays a collection of large, 3-5 μ m, randomly oriented crystals in the case of the CH₃NH₃SnI₃ perovskite films, whereas both planar heterojunction and meso-superstructured CH₃NH₃PbI_{3-x}Cl_x perovskite films have been shown to be much smoother with a greater degree of surface coverage (see Fig.3b).^{23, 24} Previously, The MAPbI_{3-x}Cl_x films also exhibited non-uniform coverage, and sporadic formation of islands on top of the mesoporous oxide films.²⁵ However, with controlled crystallisation it has been possible to considerably improve the film formation.^{21, 25, 26} Conversely, in the case of a thicker mesoporous layer (400 nm) as is shown in Fig.3c, there is no visible capping layer of perovskite suggesting that all the crystallites are contained within the mesopores of the TiO₂. A

cross section of a complete device (which will be discussed later) is shown in Figure 3d. This device is fabricated with 400nm thick mesoporous TiO₂ and in the cross section shown there does not appear to be a capping crystal. The dark region within the hole transporting material (HTM) phase is likely to be a shadowing effect rather than a perovskite capping layer. Additional SEM images are shown in the ESI.

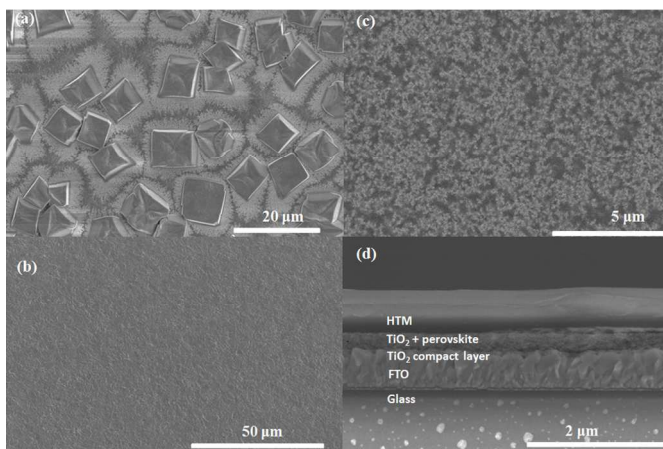


Figure 3: Scanning Electron Microscope (SEM) Images. (a) Top view of a film of CH₃NH₃SnI₃ spin-coated onto mesoporous TiO₂ (80nm thickness). (b) Top view of a film of CH₃NH₃SnI₃ spin-coated onto mesoporous TiO₂ (400 nm thickness). (c) Top view of a spin-coated film of CH₃NH₃PbI_{3-x}Cl_x on mesoporous TiO₂ (400 nm thickness). (d) Cross-sectional view of a complete device active layer composed of FTO glass/compact TiO₂ (50nm)/mesoporous TiO₂ infiltrated with CH₃NH₃SnI₃ (400nm)/Spiro-OMeTAD (600nm).

One of the main reasons why the Pb-based perovskites perform so well in planar heterojunction and meso-superstructured configurations is the sizeable diffusion length of the charge carriers.^{27, 28} In the case of these materials, the PL lifetime has been determined to be a few hundred nanoseconds for CH₃NH₃PbI_{3-x}Cl_x and at least 10 ns for the CH₃NH₃PbI₃ perovskite.^{13, 28} The presence of long-lived charge carriers allows these materials to operate efficiently in thin film architectures since the charges can be extracted from the device before significant recombination occurs, i.e., the diffusion length is much longer than the required thickness for complete light absorption. However, for CH₃NH₃SnI₃, we found the PL decay lifetime to be similar to the instrument response of our Picoquant time correlated single photon counting set up in the infrared (~200ps). Such a short PL lifetime may be due to fast recombination at either defect sites within the material, or to doped carriers resulting from the self-doping known to occur in the Sn perovskites.^{14, 29}

To probe the photophysical properties of CH₃NH₃SnI₃ in more detail we performed time resolved optical pump THz probe spectroscopy, which provides a contactless probe for the conductivity of the material at picosecond time-resolution. A single-cycle THz pulse is incident on the sample at a well-defined time-delay, after being photoexcited by a 40 fs laser pulse at 550 nm. By recording the photoinduced change of the transmitted THz amplitude, the transient conductivity of the thin-film sample can be reconstructed (see ESI for details).

Knowing the photoexcitation density from the visible pulse, we can also extract an effective charge carrier mobility.³⁰

In **Figure 5a** we display the transient photoinduced THz response of $\text{CH}_3\text{NH}_3\text{SnI}_3$ over a range of excitation fluences between $11 \mu\text{J}/\text{cm}^2$ and $108 \mu\text{J}/\text{cm}^2$. We note that the corresponding THz spectra are consistent with a conductivity of free carriers in the presence of localization effects, such as those arising from backscattering at crystallite boundaries³¹ (see ESI for full details).

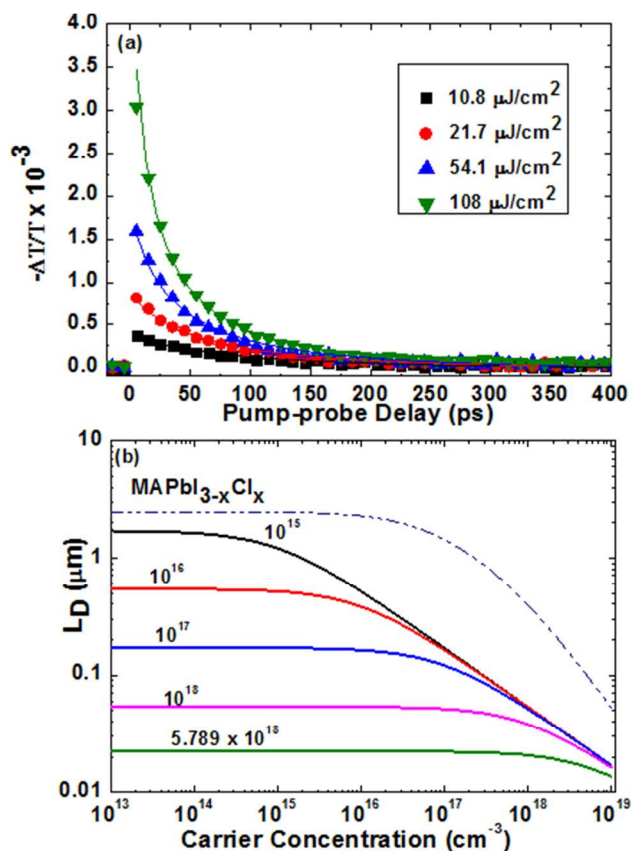


Figure 5: Terahertz (THz) Spectroscopy. (a) Transient terahertz photoconductivity of $\text{CH}_3\text{NH}_3\text{SnI}_3$ on 80 nm thick TiO_2 for a range of excitation fluences. Symbols represent experimental data while solid lines are fits to the data using the model described in the text. (b) Diffusion length (L_D) against the carrier concentration, n , for different hole doping levels as predicted from the model described in the text based on the rate constants extracted from fits to the data shown in (a) and neglecting trap-induced charge recombination. A decrease in the background level of doped holes corresponds to an increase in the diffusion length of the $\text{CH}_3\text{NH}_3\text{SnI}_3$ perovskite. The dash-dotted line displays the diffusion length of the related, as prepared lead-based perovskite $\text{CH}_3\text{NH}_3\text{PbI}_{3-x}\text{Cl}_x$ on mesoporous Al_2O_3 (from Ref.³⁰) for comparison.

Previous Hall measurements on $\text{CH}_3\text{NH}_3\text{SnI}_3$ have revealed about eight times higher mobilities, μ , for electrons than for holes; therefore we expect that the transient THz response due to photoexcited carriers is dominated by free electrons.¹⁸ We extract an effective free carrier mobility of $\varphi\mu = 1.6 \text{ cm}^2 \text{ V}^{-1} \text{ s}^{-1}$, where φ is the photon-to-free-charge conversion ratio, the precise value of which is unknown (see

ESI). We note, however, that the likelihood of immediate generation of excitons as opposed to free carriers is small due to the high non-resonant excitation about 0.6 eV above the band gap energy, such that φ is likely to be close to unity.

Earlier conductivity studies on bulk $\text{CH}_3\text{NH}_3\text{SnI}_3$ show strong levels of p-type self-doping due to the presence of Sn^{4+} impurities, on the order of $10^{16} - 10^{18} \text{ cm}^{-3}$ ^{14, 29, 32}. From our THz measurements we also observe a much faster monomolecular recombination rate than that which was observed with the Pb-based $\text{CH}_3\text{NH}_3\text{PbI}_{3-x}\text{Cl}_x$ perovskite. Therefore, assuming that the decay of the photoexcited electron population is predominantly governed by direct recombination with photoexcited and doped holes we obtain the rate equation

$$\frac{dn}{dt} = -\gamma n(p + p_0) = -\gamma np - \gamma np_0$$

which we fitted simultaneously to the fluence-dependent THz conductivity transients (solid lines in Fig. 5a, full details in ESI). We note that the first term on the RHS of equation 1 represents bimolecular recombination between photogenerated carriers, while the second term describes a monomolecular recombination between photogenerated electrons with the fixed concentration, p_0 , of dopant holes. We extract a value of $\varphi\gamma = 1.4 \times 10^{-9} \text{ cm}^3 \text{ s}^{-1}$ for the electron-hole bimolecular recombination rate constant, and a monomolecular decay constant of $\gamma p_0 = 8.08 \times 10^9 \text{ s}^{-1}$ from which we derive a hole-doping density of $\varphi^{-1}p_0 = 5.8 \times 10^{18} \text{ cm}^{-3}$. Notably the value for p_0 is at the higher end of that reported in previous studies, consistent with a significant extent of self-doping.²⁹

With the knowledge of the charge-carrier mobility and the recombination rates, we are able to derive a charge-diffusion length of 30 nm under realistic device operating conditions (see ESI for details). This value falls substantially short of the diffusion length of over 1 micron reported for $\text{CH}_3\text{NH}_3\text{PbI}_{3-x}\text{Cl}_x$,^{27, 30} suggesting that the Sn-based material, as prepared here, is unlikely to function well as a solar cell absorber in a planar heterojunction architecture, and should hence require a distributed heterojunction. These measurements were taken for $\text{CH}_3\text{NH}_3\text{SnI}_3$ coated on 80 nm thick films of mesoporous TiO_2 , similar values were obtained for $\text{CH}_3\text{NH}_3\text{SnI}_3$ coated upon 80 nm thick films of mesoporous Al_2O_3 (See ESI, **Figure S5**).

Since we know the effective mobility, the bimolecular recombination rate constant, and have an estimate of the background concentration of doped holes, we can extrapolate how the diffusion length would change if the background concentration of doped holes were to be decreased (see ESI for details). In Fig. 5b, we show a graph of simulated diffusion length against photoexcited carrier concentration for five different doped hole concentrations. For comparison a plot of the actual diffusion length of the as prepared Pb analogue ($\text{CH}_3\text{NH}_3\text{PbI}_{3-x}\text{Cl}_x$) is added. We show here that if the background doping level in the $\text{CH}_3\text{NH}_3\text{SnI}_3$ perovskite were to be decreased to the order of 10^{15} cm^{-3} , then the diffusion length could increase beyond a micron in length and approach that of the very efficient Pb-based perovskite system. This result is a direct consequence of the low bi-molecular recombination rate observed for the material, which is similarly low compared to the value previously determined for the Pb-based counterpart.

Despite the slightly lower THz carrier mobility, this rate is still short of the prediction of the Langevin model by a factor $5 \times 10^4 \times \epsilon^{-1}$, with ϵ being the relative permittivity of the material. Our observations clearly identify a reduction of self-doping as a promising strategy to enhance

the carrier lifetime and hence, prospects for efficient photovoltaic operation. With the knowledge of the short diffusion length, we fabricated perovskite-sensitized solar cells (PSSCs), composed of FTO coated glass/ compact TiO₂/ mesoporous TiO₂ (400nm) coated with the CH₃NH₃SnI₃/Spiro-OMeTAD/Au. The entire device was assembled in a nitrogen-filled glovebox after which the devices were transferred to the evaporator located within the glovebox, hence avoiding exposure to air. Encapsulation was subsequently performed under the same conditions using a hot melt polymer laminate with a glass coverslip,

and epoxy resin to seal around the edges. This was done so that the device was exposed to negligible levels of oxygen or moisture during fabrication. The sealed cells were then removed from the glove box and immediately measured in air. Control devices using the Pb-based perovskite as an absorber were also fabricated in the glovebox and tested in the same manner, but without encapsulation. Device performance parameters from a batch of cells, along with the current-voltage characteristics of the best devices, are presented in **Figure 4**. Current-voltage characteristics for devices with varying performance are shown in the ESI.

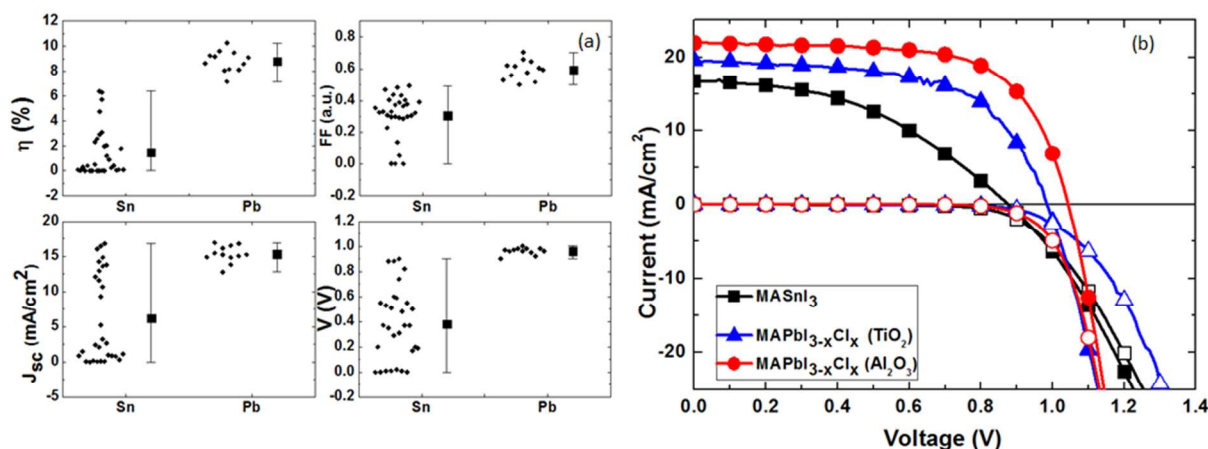


Figure 4: Current-Voltage Characteristics and Device Performance Parameters. (a) The solar cell performance parameters extracted from measuring current-voltage curves under AM1.5 simulated sun light of 100mWcm⁻² for TiO₂-based perovskite sensitized solar cells employing CH₃NH₃SnI₃ (Sn) and CH₃NH₃PbI_{3-x}Cl_x (Pb) absorbers. (b) Current-voltages curves of the best Sn-based and Pb-based devices for the batch of devices shown in (a). Light JV curves are denoted with solid symbols and the dark IV curves with hollow symbols. The Pb-based perovskite is shown both on TiO₂ (blue curve) and Al₂O₃ (red curve) giving short circuit currents (J_{sc}) of 19.6 mAcm⁻² and 21.9 mAcm⁻², open circuit voltages (V_{oc}) of 0.98 V and 1.04 V, fill factors (FF) of 0.60 and 0.66, and power conversion efficiencies (η) of 11.5 % and 15.0% respectively. While the Sn-based perovskite showed negligible photovoltaic properties on Al₂O₃, on TiO₂ a maximum η of 6.4% was obtained, corresponding to a V_{oc} of 0.88 V, J_{sc} of 16.8 mAcm⁻² and FF of 0.42. It is important to note that the Sn-based devices were fabricated, metal electrodes evaporated and devices sealed in a nitrogen filled glove box prior to exposing to air.

There is a broad spread in the performance of the CH₃NH₃SnI₃ solar cells. Here we show that the best performing Sn-based device reaches a power efficiency of 6.4% under 1-sun illumination. Quite remarkably, for an absorber with a bandgap of 1.23 eV, the open circuit voltages reach values as high as 0.88 V in the most efficient device. The fundamental energy loss in a photovoltaic system can be taken as the difference between the bandgap and the open-circuit voltage obtained.³³ For crystalline silicon solar cells, which currently dominate the market, this loss is approximately 0.35 eV, while for GaAs, our closest example of a perfectly ordered crystalline material, the loss is in the range of 0.27 eV.^{3, 34, 35} Here, the loss we estimate is only 0.35 eV in the best performing cells, which matches that of c-Si.³⁶

Observing such high open-circuit voltages in these solar cells is unexpected considering the relatively short lifetime and hence diffusion length, as well as the use of mesoporous TiO₂,

which has previously resulted in lower open-circuit voltages in CH₃NH₃PbI_{3-x}Cl_x solar cells.^{5, 37} However, if the low diffusion length is a consequence of the fast recombination to doped carriers as we infer, then this will not necessarily impede the open-circuit voltage. The inferred high p-doping density (10¹⁸cm⁻³) is much higher than the photo-induced charge density under full sun light (<10¹⁵ cm⁻³ for the Pb-based perovskite).^{27, 38} This implies that under open-circuit conditions where no holes can be swept out of the device, the quasi Fermi level for holes will be very close to the valence band edge. Provided that electrons can transfer quickly and efficiently to the TiO₂, in principle the quasi Fermi level for electrons may be set by the Fermi level in the TiO₂. The additional surprise is that the mesoporous TiO₂ would also have to become comparably doped to enable the quasi Fermi level for electrons to be close to the conduction band, which is required to sustain such a high open-circuit voltage under illumination.

In **Figure S4** we show a zoom-in of the dark current-voltage curves, and we note that the dark current for the best device only exhibits marginally more leakage at low bias (0 to 0.6 V) than the Pb based perovskite solar cells. However, for the poorer performing cells the dark current leakage is significant, as we show in **Figure S5**, and is largely responsible for the wide spread in open-circuit voltage. It is likely that there is a range of doping densities within the as prepared and tested devices which could account for this variable dark current leakage. Evidently, this does require further investigation. While one would expect higher short-circuit currents from a low band gap system such as this, a major factor which would inhibit both the J_{sc} and the FF is the short electron diffusion length. We have identified that this is likely to be due to excessive self-doping, but with appropriate control of this phenomenon, coupled with improved control of the thin film processing, these early solar cell results are very promising. We must note however, that even with encapsulation the devices still quickly degrade when tested under ambient conditions. Within minutes of measuring, a deeply coloured device can become completely transparent. X-ray diffraction measurements of the degraded solar cells, which we show in SI, indicate complete degradation of the perovskite structure. This is indicative of either our current device sealing protocol failing to prevent oxygen/ moisture from causing device degradation or a fundamental instability of the material.

In the devices, we employ metal electrodes to extract the current, and it is not possible with our current configuration to completely seal beneath the electrodes. Hence oxygen and moisture could ingress the film through the active layer beneath the electrodes. In order to determine if complete sealing would inhibit the rapid degradation, we processed $\text{CH}_3\text{NH}_3\text{SnI}_3$ films on large glass substrates and scraped all the material away from the edge of the glass slides. We then completely sealed the slides with the hot-melt polymer film, a glass cover slide and edge sealed with epoxy resin. These films were subject to a continuous light soaking over a 4-month period. After 4 months the films were still visibly coloured, as we show in Figure S1, and there was no significant drop in their absorbance indicating that with appropriate current extraction and sealing protocol, predominant stabilisation should be possible.

3. Conclusions

In summary, we have provided the first demonstration of an efficient, completely lead-free perovskite solar cell using the Sn-based perovskite, $\text{CH}_3\text{NH}_3\text{SnI}_3$ as the absorber layer. This shows that good photovoltaic performance and unexpectedly high open-circuit voltage is not strictly limited to lead-based perovskites. These devices yielded efficiencies of more than 6%, however the stability of $\text{CH}_3\text{NH}_3\text{SnI}_3$ remains a challenge.

The voltage losses in the material appear to be remarkably low, suggesting that when its full potential is exploited, the efficiencies could very well approach those of c-Si and GaAs. We have determined the mobility of the as prepared films to be approximately $1.6 \text{ cm}^2 \text{ V}^{-1} \text{ s}^{-1}$ and the diffusion length to be approximately 30 nm as compared to over a micron in the Pb-based perovskites, $\text{CH}_3\text{NH}_3\text{PbX}_3$.^{27, 28, 30} However, the diffusion length is limited by recombination with self-doping carriers, and if the background concentration of holes were to be decreased, then the diffusion length could approach 1 micron, opening the possibility for planar heterojunction devices. The pivotal issue is now the stabilisation of the material such that the oxidation of the Sn within the crystal is suppressed, thus reducing the doping levels of the material and enabling long term stable operation. By achieving a solution to this, we may see the performance of Sn perovskites surpassing those of the state-of-the-art Pb-based perovskites over the next few years, with a distinct toxicology advantage.

4. Experimental

Device Fabrication

Briefly, FTO-coated glass sheets ($7 \Omega \text{ cm}^{-1}$ Pilkington) were etched with zinc powder and HCl (3M) to obtain the required electrode pattern. The sheets were then washed with soap (2% Hellmanex in water), deionized water, acetone, and methanol, and finally treated under oxygen plasma for 10 min to remove the last traces of organic residues. All chemicals were purchased from Sigma Aldrich and used as received unless otherwise stated. A 100 nm thick compact layer of TiO_2 was then deposited on the glass using titanium isopropoxide (99.999% purity) diluted in anhydrous ethanol and sintered for 45 mins at 500°C . After the substrate was allowed to cool, a 400 nm thick layer of TiO_2 (Dyesol 18 NRT) was deposited via spin coating at 2000 rpm for 1 min. The substrate was then resintered at 500°C for 45 min.

The $\text{CH}_3\text{NH}_3\text{SnI}_3$ perovskite precursor solution was prepared by dissolving equimolar quantities of $\text{CH}_3\text{NH}_3\text{I}$ and SnI_2 to a concentration of 40 wt% in N-dimethylformamide (DMF). The precursor solution was then spin coated onto the TiO_2 coated substrate under inert atmosphere. The perovskite layer formed during spin coating. After formation of the perovskite layer, the hole transporting material (HTM) 2,2',7,7'-tetrakis(N,N'-di-p-methoxyphenylamine)-9,9'-spirobifluorene (spiro-OMeTAD) was dissolved in (concentration 80 mM) with addition of additives at a concentration of 10 mM hydrogen bis(trifluoromethanesulfonyl)imide (H-TFSI) and 80mM tert-butylpyridine (tBP).³⁹ We note that the additives combination commonly used with spiro-OMeTAD, 15 mM of lithium bis(trifluoromethylsulfonyl)imide salt (Li-TFSI) and 70 mM of 4-tert-butylpyridine (tBP), made the $\text{CH}_3\text{NH}_3\text{SnI}_3$ more unstable than H-TFSI. Lastly, 50 nm thick gold electrodes

were evaporated onto the devices through a shadow mask, using a thermal evaporator giving an effective active area of $\sim 0.12 \text{ cm}^2$ as defined by the overlap of the gold and FTO electrodes. The devices were then sealed under inert atmosphere, using a meltable polymer and an epoxy resin.

Solar Cell Characterization

Solar cell performance was measured using a class AAB ABET solar simulator which was calibrated to give simulated AM 1.5 sunlight at an irradiance of 100 mW/cm^2 . The irradiance was calibrated using an NREL-calibrated KG5 filtered silicon reference cell. Current-Voltage curves were recorded using a sourcemeter (Keithley 2400, USA). All solar cells were masked with a metal aperture which was used to define the active area of the devices, which in this case was 0.0625 cm^2 .

Optical Characterization

Samples for optical characterisation were prepared using a similar precursor solution as for the devices. A 1:2 dilution of Al_2O_3 nanoparticles in isopropanol was spin coated onto a glass slide, resulting in a layer which was 80 nm thick. The Sn-perovskite precursor solution was then spin coated onto the substrate at 2000 rpm, under inert atmosphere. After the formation of the perovskite, the slides were sealed in the same manner as the devices. The steady-state absorption spectra were acquired with a Perkin-Elmer Lambda 1050 UV/Vis/NIR spectrophotometer using an integrating sphere to account for reflection and scattering. We note however that the films were located on the front and back of the integrating sphere for the transmission and reflection measurements and severe scattering out of the sides of the substrates escapes the integrating sphere and will hence erroneously appear as an absorption.

Steady-state photoluminescence (PL) measurements were taken using an automated spectrofluorometer (Fluorolog, Horiba Jobin-Yvon), with a 450 W Xenon lamp excitation source and liquid nitrogen cooled InGaAs NIR detector for $\text{CH}_3\text{NH}_3\text{SnI}_3$ samples and a photomultiplier tube detector for $\text{CH}_3\text{NH}_3\text{PbI}_{3-x}\text{Cl}_x$ samples. The excitation wavelength was 500 nm. All spectra were corrected for instrumental response using a calibration lamp of known emissivity.

Photothermal Deflection Spectroscopy

Photothermal Deflection Spectroscopy (PDS) is a highly sensitive surface averaged absorption measurement technique. Full details about this experiment are described elsewhere.⁴⁰ For this measurement 300 nm thick $\text{CH}_3\text{NH}_3\text{SnI}_3$ perovskite layers were spin coated onto quartz substrates from the precursor solution.

THz Time Domain Spectroscopy

Full experimental detail is given elsewhere. The optical-pump-THz-probe setup uses a Ti:Sapphire regenerative amplifier to generate 40 fs pulses at 800 nm wavelength and a repetition

rate of 1.1 kHz. Terahertz pulses are generated by optical rectification in 450 μm thick (110)-GaP and detected by electro-optic sampling in a ZnTe crystal (0.2 mm (110)-ZnTe on 3 mm (100)-ZnTe). Pulses for optical excitation of the samples at a wavelength of 550 nm have been generated using an optical parametric amplifier (OPA). Optical excitation was carried out from the non-substrate side of the film. The diameters of pump and probe beam at the sample position are 4.2 mm and 1.5 mm (FWHM). Measurements have been performed with the entire THz beam path (including emitter, detector and sample) in an evacuated chamber at pressure of $< 10^{-1}$ mbar.

Acknowledgements

This work was supported by EPSRC and the European Research Council (ERC) HYPER PROJECT no. 27988. N.N. thanks the Government of the Republic of Trinidad and Tobago for additional financial support. The authors would like to thank Dr. James M. Ball for device photography and helpful discussions; Dr. Martina Congiu for SEM images; and Sir Professor Richard Friend and Severin N. Habisreutinger for helpful discussions.

Notes and references

- ^a Clarendon Laboratory, Department of Physics, University of Oxford, Parks Road, Oxford, OX1 3PU, United Kingdom
^b Italian Institute of Technology, Centre for Nano Science and Technology, Politecnico di Milano, Via Pascoli 70/3, 20133 Milan, Italy
^c Dipartimento di Fisica, Politecnico di Milano, Piazza L. da Vinci 32, 20133 Milan, Italy.
^d Cavendish Laboratory, Department of Physics, University of Cambridge, 19 JJ Thomson Ave, Cambridge, CB3 0HE, United Kingdom
 Electronic Supplementary Information (ESI) available: Additional experimental detail, XRD and photographs of degraded $\text{CH}_3\text{NH}_3\text{SnI}_3$, additional cross-sectional and top view images, terahertz absorption and conductivity on 80 nm Al_2O_3 as well as details of the terahertz modelling are all available. See DOI: 10.1039/b000000x/

1. C. Steven and M. Arun, *Nature*, 2012, **488**, 294-303.
2. A. Yella, H.-W. Lee, H. N. Tsao, C. Yi, A. K. Chandiran, M. K. Nazeeruddin, E. W.-G. Diau, C.-Y. Yeh, S. M. Zakeeruddin and M. Grätzel, *Science*, 2011, **334**, 629-634.
3. M. A. Green, K. Emery, Y. Hishikawa, W. Warta and E. D. Dunlop, *Progress in Photovoltaics: Research and Applications*, 2014, **22**, 1-9.
4. J. A. Chang, S. H. Im, Y. H. Lee, H.-j. Kim, C.-S. Lim, J. H. Heo and S. I. Seok, *Nano Letters*, 2012, **12**, 1863-1867.
5. M. M. Lee, J. Teuscher, T. Miyasaka, T. N. Murakami and H. J. Snaith, *Science*, 2012, **338**, 643-647.
6. J. Burschka, N. Pellet, S.-J. Moon, R. Humphry-Baker, P. Gao, M. K. Nazeeruddin and M. Grätzel, *Nature*, 2013, **499**, 316-319.
7. M. Liu, M. B. Johnston and H. J. Snaith, *Nature*, 2013, **501**, 395-398.
8. O. Malinkiewicz, A. Yella, Y. H. Lee, G. M. Espallargas, M. Graetzel, M. K. Nazeeruddin and H. J. Bolink, *Nat Photon*, 2014, **8**, 128-132.
9. A. Kojima, K. Teshima, Y. Shirai and T. Miyasaka, *Journal of the American Chemical Society*, 2009, **131**, 6050-6051.
10. J.-H. Im, C.-R. Lee, J.-W. Lee, S.-W. Park and N.-G. Park, *Nanoscale*, 2011, **3**, 4088-4093.

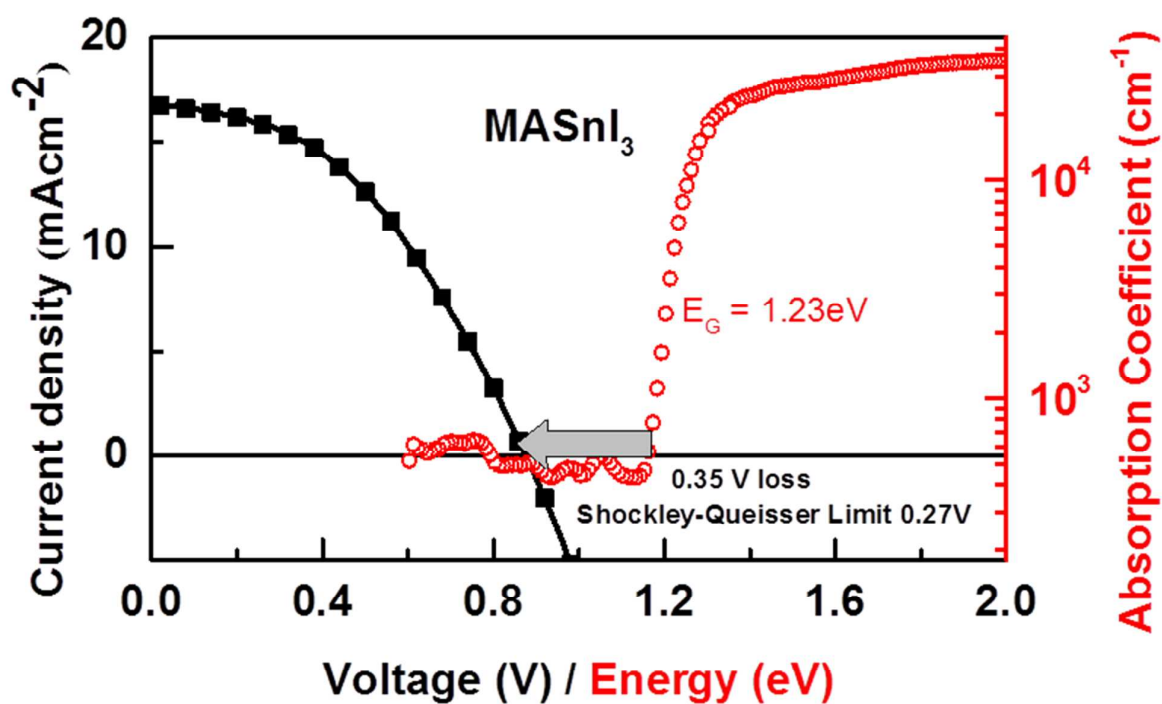
11. J. H. Noh, S. H. Im, J. H. Heo, T. N. Mandal and S. I. Seok, *Nano Letters*, 2013, **13**, 1764-1769.
12. N. R. E. L. (NREL), NREL, www.nrel.gov/ncpv/images/efficiency_chart.jpg.
13. C. R. Kagan, D. B. Mitzi and C. D. Dimitrakopoulos, *Science*, 1999, **286**, 945-947.
14. Y. Takahashi, R. Obara, Z.-Z. Lin, Y. Takahashi, T. Naito, T. Inabe, S. Ishibashi and K. Terakura, *Dalton Transactions*, 2011, **40**, 5563-5568.
15. D. B. Mitzi, C. A. Feild, Z. Schlesinger and R. B. Laibowitz, *Journal of Solid State Chemistry*, 1995, **114**, 159-163.
16. Y. Ogomi, A. Morita, S. Tsukamoto, T. Saitho, N. Fujikawa, Q. Shen, T. Toyoda, K. Yoshino, S. S. Pandey, T. Ma and S. Hayase, *The Journal of Physical Chemistry Letters*, 2014, 1004-1011.
17. J. M. Ball, M. M. Lee, A. Hey and H. Snaith, *Energy & Environmental Science*, 2013.
18. C. C. Stoumpos, C. D. Malliakas and M. G. Kanatzidis, *Inorganic Chemistry*, 2013, **52**, 9019-9038.
19. C. Wehrenfennig, M. Liu, H. J. Snaith, M. B. Johnston and L. M. Herz, *The Journal of Physical Chemistry Letters*, 2014, 1300-1306.
20. S. De Wolf, J. Holovsky, S.-J. Moon, P. Löper, B. Niesen, M. Ledinsky, F.-J. Haug, J.-H. Yum and C. Ballif, *The Journal of Physical Chemistry Letters*, 2014, **5**, 1035-1039.
21. G. E. Eperon, S. D. Stranks, C. Menelaou, M. B. Johnston, L. M. Herz and H. J. Snaith, *Energy & Environmental Science*, 2014, **7**, 982-988.
22. E. Edri, S. Kirmayer, D. Cahen and G. Hodes, *The Journal of Physical Chemistry Letters*, 2013, **4**, 897-902.
23. K. W. Tan, D. T. Moore, M. Saliba, H. Sai, L. A. Estroff, T. Hanrath, H. J. Snaith and U. Wiesner, *ACS Nano*, 2014.
24. M. Saliba, K. W. Tan, H. Sai, D. T. Moore, T. Scott, W. Zhang, L. A. Estroff, U. Wiesner and H. J. Snaith, *The Journal of Physical Chemistry C*, 2014.
25. G. E. Eperon, V. M. Burlakov, P. Docampo, A. Goriely and H. J. Snaith, *Advanced Functional Materials*, 2014, **24**, 151-157.
26. B. Conings, L. Baeten, C. De Dobbelaere, J. D'Haen, J. Manca and H.-G. Boyen, *Advanced Materials*, 2014, **26**, 2041-2046.
27. S. D. Stranks, G. E. Eperon, G. Grancini, C. Menelaou, M. J. P. Alcocer, T. Leijtens, L. M. Herz, A. Petrozza and H. J. Snaith, *Science*, 2013, **342**, 341-344.
28. G. Xing, N. Mathews, S. Sun, S. S. Lim, Y. M. Lam, M. Grätzel, S. Mhaisalkar and T. C. Sum, *Science*, 2013, **342**, 344-347.
29. Y. Takahashi, H. Hasegawa, Y. Takahashi and T. Inabe, *J. Solid State Chem.*, 2013, **205**, 39-43.
30. C. Wehrenfennig, G. E. Eperon, M. B. Johnston, H. J. Snaith and L. M. Herz, *Advanced Materials*, 2014, **26**, 1584-1589.
31. H. Němec, P. Kužel and V. Sundström, *Phys. Rev. B*, 2009, **79**, 115309.
32. D. B. Mitzi, C. A. Feild, Z. Schlesinger and R. B. Laibowitz, *J. Solid State Chem.*, 1995, **114**, 159-163.
33. H. J. Snaith, *Advanced Functional Materials*, 2010, **20**, 13-19.
34. P. K. Nayak, J. Bisquert and D. Cahen, *Advanced Materials*, 2011, **23**, 2870-2876.
35. P. K. Nayak and D. Cahen, *Advanced Materials*, 2014, **26**, 1622-1628.
36. W. Shockley and H. J. Queisser, *Journal of Applied Physics*, 1961, **32**, 510-519.
37. T. Leijtens, B. Lauber, G. E. Eperon, S. D. Stranks and H. J. Snaith, *The Journal of Physical Chemistry Letters*, 2014, **5**, 1096-1102.
38. V. D'Innocenzo, G. Grancini, M. J. P. Alcocer, A. R. S. Kandada, S. D. Stranks, M. M. Lee, G. Lanzani, H. J. Snaith and A. Petrozza, *Nat Commun*, 2014, **5**.
39. A. Abate, D. J. Hollman, J. Teuscher, S. Pathak, R. Avolio, G. D'Errico, G. Vitiello, S. Fantacci and H. J. Snaith, *Journal of the American Chemical Society*, 2013, **135**, 13538-13548.
40. A. J. Kronemeijer, V. Pecunia, D. Venkateshvaran, M. Nikolka, A. Sadhanala, J. Moriarty, M. Szumilo and H. Siringhaus, *Advanced Materials*, 2014, **26**, 728-733.

Lead-Free Organic-Inorganic Tin Halide Perovskites for Photovoltaic Applications

Nakita K. Noel,¹ Samuel D. Stranks,¹ Antonio Abate,¹ Christian Wehrenfennig,¹ Simone Guarnera,^{2,3} Amir Abbas Haghighirad,¹ Aditya Sadhanala,⁴ Giles E. Eperon,¹ Sandeep K. Pathak,¹ Michael B. Johnston,¹ Anna Maria Petrozza,² Laura M. Herz,¹ Henry J. Snaith^{1*}

Broad Context:

The resource for photovoltaic solar energy, namely sun light, is ubiquitous across the globe, predictable and in excess of our required power demand by many orders of magnitude. The current solar industry is dominated by crystalline silicon, which converts sun light to electrical energy at around 20% efficiency. The cost of silicon PV has dropped considerably over the last 5 years, and is rapidly approaching the cost of generating electricity from fossil fuels. However, PV will only emerge as the primary power source if the cost can be lowered further to become cheaper than generating electricity from coal. Organic-inorganic crystalline perovskite materials have in the last two years proliferated the PV research community and solar cells based on these materials promise to reach the same efficiencies as crystalline silicon, but at a fraction of the cost. However, the presence of lead in the semiconductor has raised questions as to whether toxicology issues will become problematic in the future for widespread deployment of this technology. Here, we have demonstrated for the first time efficient operation of an entirely lead-free perovskite solar cell, illustrating that there is no uniqueness to lead, and beckoning even higher efficiencies for non-toxic, abundant low cost solar cells.



Lead-Free Organic-Inorganic Tin Halide Perovskites for Photovoltaic Applications

Nakita K. Noel,¹ Samuel D. Stranks,¹ Antonio Abate,¹ Christian Wehrenfennig,¹ Simone Guarnera,^{2,3} Amir Abbas Haghhighirad,¹ Aditya Sadhanala,⁴ Giles E. Eperon,¹ Sandeep K. Pathak,¹ Michael B. Johnston,¹ Anna Maria Petrozza,² Laura M. Herz,¹ Henry J. Snaith^{1*}

¹ Clarendon Laboratory, Department of Physics, University of Oxford, Parks Road, Oxford, OX1 3PU, United Kingdom

² Italian Institute of Technology, Centre for Nano Science and Technology, Politecnico di Milano, Via Pascoli 70/3, 20133 Milan, Italy

³ Dipartimento di Fisica, Politecnico di Milano, Piazza L. da Vinci 32, 20133 Milano, Italy

⁴ Cavendish Laboratory, Department of Physics, University of Cambridge, 19 JJ Thomson Ave, Cambridge, CB3 0HE, United Kingdom

*Corresponding author: Henry J. Snaith, e-mail: h.snaith1@physics.ox.ac.uk

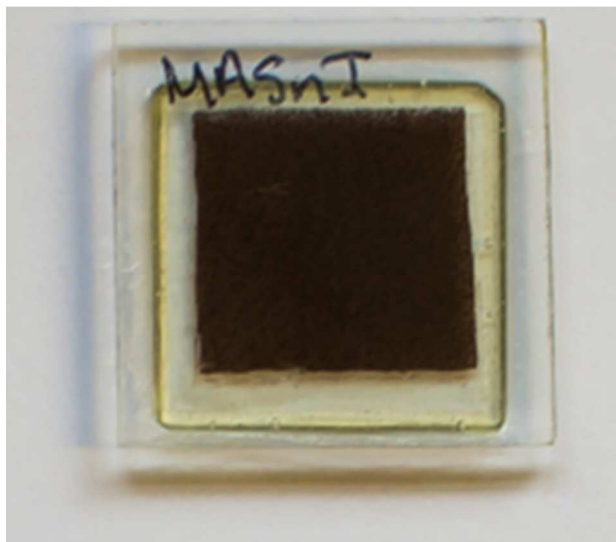
SUPPORTING INFORMATION

Figure S1- Photograph showing a film of the black/brown, CH₃NH₃SnI₃. This film was sealed in a nitrogen filled glove box and has been aged for 4 months under AM1.5 76mWcm⁻² sun light generated from a sun-test CPSPlus light soaking box.

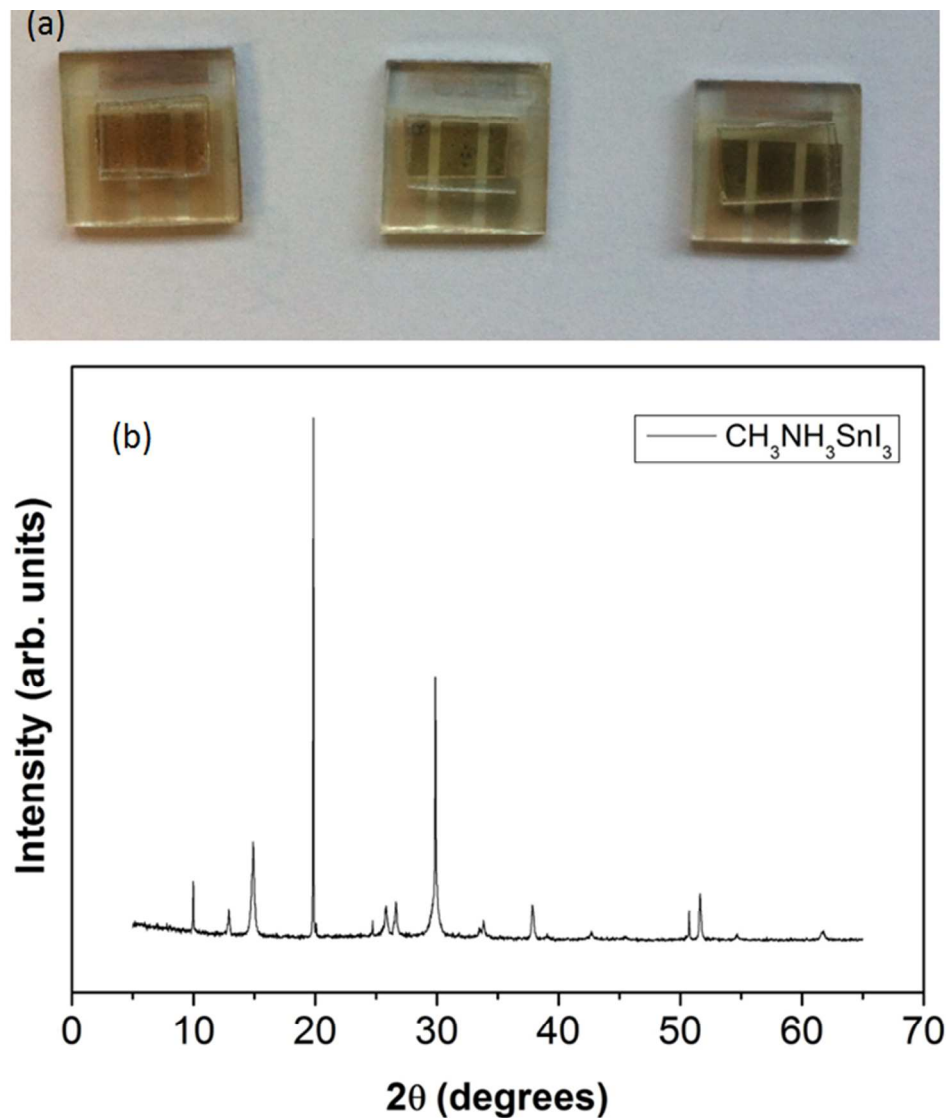


Figure S2: (a) Photograph showing solar cell devices where the $\text{CH}_3\text{NH}_3\text{SnI}_3$ absorber layer has degraded. (b) X-ray Diffractogram of a degraded sample of $\text{CH}_3\text{NH}_3\text{SnI}_3$.

X-ray Diffraction

The X-ray diffraction pattern shown above corresponds to methylammonium iodide with some impurities. The lattice parameters derived were as follows: $a = 11.2246 \text{ \AA}$ and $c = 8.9362 \text{ \AA}$.

While we note that there are no visible peaks for any oxides of tin, this is quite likely due to the formation of amorphous species which will not be clearly detected by this measurement.

Scanning Electron Microscopy (SEM) Images

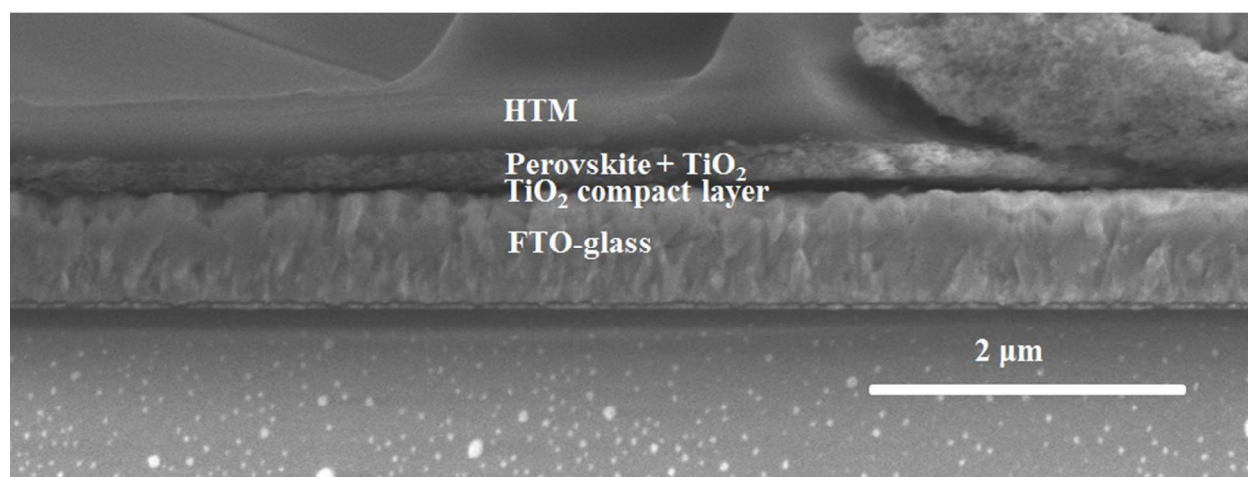


Figure S3: Cross-Sectional Scanning Electron Microscope (SEM) Image. Cross-sectional SEM image of a TiO₂-based CH₃NH₃SnI₃ device.

The cross-sectional SEM image above shows clearly that there is no capping layer of perovskite formed by CH₃NH₃SnI₃ in this device configuration. In a device with a 400 nm thick mesoporous TiO₂, the perovskite material is contained solely within the pores of the TiO₂. The delamination of the TiO₂ layer is as a result of fracturing the device. The formation of a capping layer in such a device is undesirable as a result of the short diffusion length of the material, which will cause recombination to occur on a faster timescale than charge extraction. Top view images of both 80 nm thick and 400 nm thick TiO₂ films infiltrated with CH₃NH₃SnI₃ are shown

below. This image very accurately illustrates the loss of the capping layer with increased film thickness.

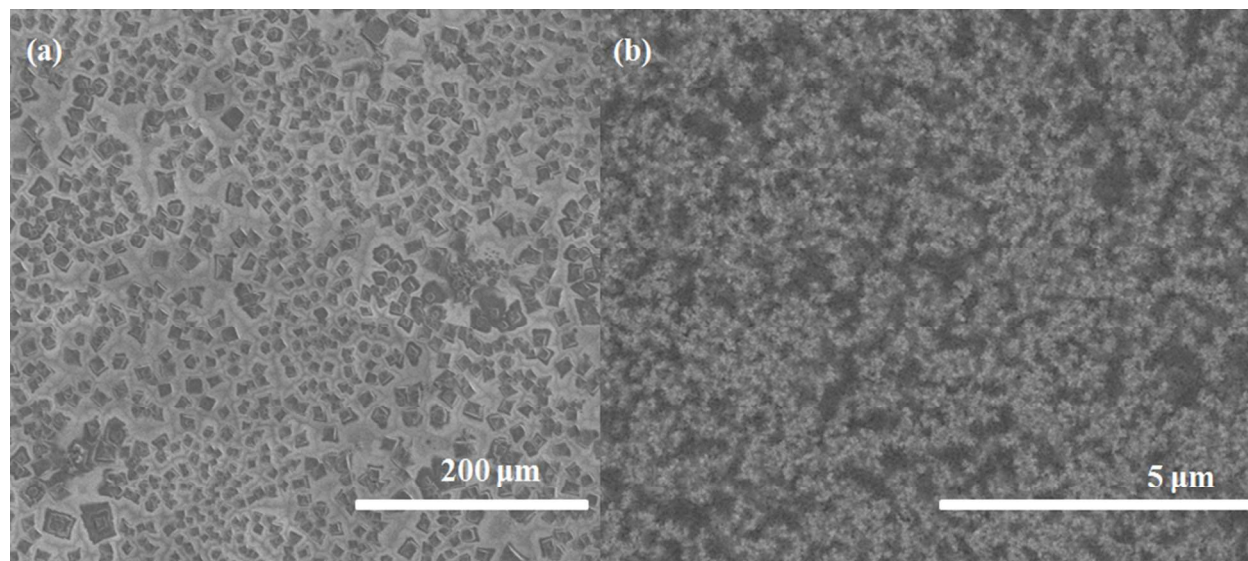


Figure S4: Top-View Scanning Electron Microscope Images. Top view SEM image of (a) A capping layer of disperse $\text{CH}_3\text{NH}_3\text{SnI}_3$ crystal formed on an 80 nm thick film of TiO_2 . (b) $\text{CH}_3\text{NH}_3\text{SnI}_3$ coated on a 400 nm thick film of TiO_2 such that all of the crystallites have formed within the pores of the TiO_2 and no capping layer is present.

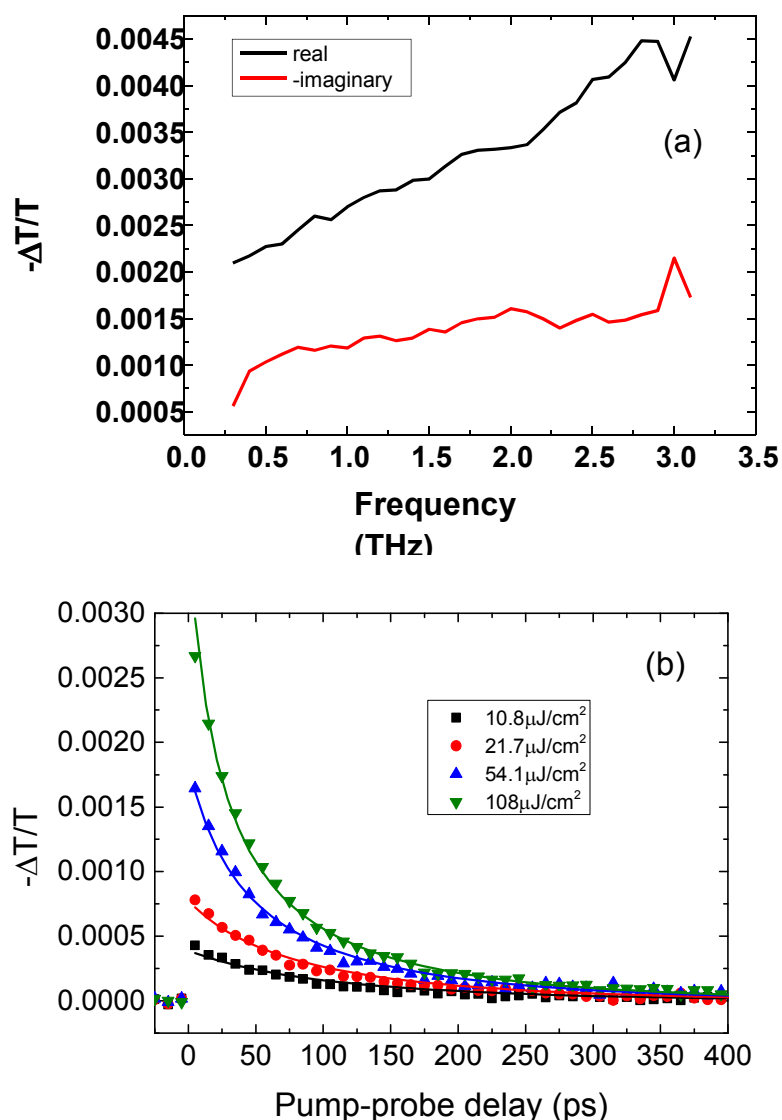


Figure S3: Terahertz spectroscopy. (a) Terahertz photo induced absorption spectrum (obtained through inverse Fourier Transform of the time-domain response $\Delta T(t)/T(t)$) for a sample of $\text{CH}_3\text{NH}_3\text{SnI}_3$ on 80-nm thick mesoporous TiO_2 (excitation wavelength: 550 nm, fluence $108 \mu\text{J}/\text{cm}^2$). (b) Transient terahertz photoconductivity of $\text{CH}_3\text{NH}_3\text{SnI}_3$ on 80-nm thick mesoporous Al_2O_3 at a range of excitation fluences (excitation wavelength: 550 nm). Symbols represent experimental data while solid lines are fits to the data using the model described in the

text. We extract an effective free carrier mobility of $\phi\mu = 1.58 \text{ cm}^2 \text{ V}^{-1} \text{ s}^{-1}$, a bimolecular rate constant of $\phi\gamma = 1.01 \times 10^{-9} \text{ cm}^3 \text{ s}^{-1}$, and hole-doping density of $p_0 = 6.39 \times 10^{18} \text{ cm}^{-3}$

THz Time-Domain Spectroscopy

Figure S3a shows the frequency-spectrum of the complex photoinduced THz conductivity recorded at a pump-probe delay of 20 ps. We note that no change in the spectral shape with time is observed and hence the data shown are representative of the entire investigated timescale. The spectrum can clearly not be described by a simple Drude-like free-carrier response. The data are however consistent with the THz conductivity of free carriers in the presence of localization effects, such as those arising from backscattering at crystallite boundaries (1). A similar spectral response to the one observed here has e.g. been found in sintered TiO_2 nanoparticle films (1) (2). While an excitonic resonance would be able to explain the rise in the real part of the THz spectrum towards higher frequencies, it is not consistent with a non-zero imaginary part at low-frequencies. Hall measurements on $\text{CH}_3\text{NH}_3\text{SnI}_3$ have revealed about eight times higher mobilities for electrons than for holes; therefore we expect that the transient THz response due to photoexcited carriers is dominated by free electrons (3).

Derivation of photoconductivity and charge carrier mobility from the change in THz electric field transmission

The sheet photoconductivity ΔS of a thin film between two media of refractive indices n_A and n_B , under the condition that the thickness of the film is much smaller than the THz wavelength, may be expressed as (4) (5)

$$\Delta S = -\epsilon_0 c (n_A + n_B) \left(\frac{\Delta T}{T} \right), \quad (1)$$

where $\Delta T = T_{\text{illuminated}} - T$ is the photoinduced change in terahertz electric field. Here, T and $T_{\text{illuminated}}$ are the transmitted terahertz electric fields of the sample in the dark and after photoexcitation respectively. In our experiment the sample film is surrounded by vacuum from one side, hence $n_A = 1$ and in contact with the z-cut quartz substrate with THz-refractive index $n_B = 2.13$ from the other side.

In order to derive the charge-carrier mobility μ from the photoinduced sheet conductivity, the number of photo-excited charge carriers N needs to be determined using

$$N = \varphi \frac{E\lambda}{hc} (1 - R_{\text{pump}})(1 - T_{\text{pump}}) \quad (2)$$

Here, E is the energy contained in an optical excitation pulse of wavelength λ , R_{pump} is the reflectivity of the sample at normal incidence of the excitation beam, T_{pump} the (small) fraction of light transmitted through the sample and φ is the ratio of free charge carriers created per photons absorbed, commonly referred to as the photon-to-charge branching ratio, which is technically undetermined in the experiment and related to factors such as the exciton binding energy in the material. We argue however in the main manuscript that there is some evidence making it appear likely that φ is not substantially lower than unity.

The charge carrier mobility μ is given by

$$\mu = \frac{\Delta S A_{\text{eff}}}{Ne} \quad (3)$$

where A_{eff} is the effective area of the overlap of optical pump and THz probe pulse taking into account the Gaussian beam profiles, and e is the elementary charge. With φ unknown, the quantity which can be directly derived from the experiment is the effective mobility $\tilde{\mu} = \varphi\mu$ where

$$\varphi\mu = -\varepsilon_0 c (n_A + n_B) \frac{A_{\text{eff}} hc}{E e \lambda (1 - R_{\text{pump}})(1 - T_{\text{pump}})} \left(\frac{\Delta T}{T} \right) \quad (4)$$

Because $0 \leq \phi \leq 1$, the effective mobility represents a lower limit, which becomes identical to the actual mobility for full photon-to-free-carrier conversion. The determined charge carrier mobility arises from the contributions of both electrons and holes, which cannot be separated. Therefore the extracted mobility value is the sum of electron and hole mobilities.

To allow accurate determination of $\phi\mu$ we ensured that excitation conditions are in the linear regime. We have evaluated the dependence of the initial amplitude of the THz response on excitation fluence and found that nonlinear processes such as two-photon absorption do not have significant effect in the range of fluences used in this study ($\leq 110 \mu\text{J cm}^{-2}$).

Fits to THz photoconductivity transients

As described in the main manuscript, we model the decay dynamics of the photoexcited electron density $n(t)$ in terms of recombination with photoexcited and doped holes ($p(t) + p_0$). We neglect the influence of mono-molecular contributions from trap-mediated processes as well as third- or higher order processes. The former assumption can to some extent be justified from the comparison to the related lead halide materials, where trap-induced effects have been found to occur on timescales more than two orders of magnitude longer than those studies in our THz experiments (6) (7) (8). This results in the following rate equation:

$$\frac{dn}{dt} = -\gamma n(p + p_0) = -\gamma np - \gamma np_0 \quad (5)$$

Here, γ is the electron-hole recombination rate constant. Note that, since (after thermalization) photoinduced and doped holes are indistinguishable, the corresponding population is described in terms of the sum of the initial hole density before photoexcitation p_0 and the dynamic contribution $p(t)$. In this definition p_0 is equal to the doped hole density in the absence of illumination and $p(0)$ the initial photoexcited hole density (before any recombination events). Since our model only allows decay via e-h-recombination events, n and p have to follow the same time-evolution. As furthermore $n(0) = p(0)$, it follows that $n(t) = p(t)$ and therefore (5) becomes

$$\frac{dn}{dt} = -\gamma n^2 - \gamma p_0 n = -k_2 n^2 - k_1 n \quad (6)$$

with $k_2 \stackrel{\text{def}}{=} \gamma$ and $k_1 \stackrel{\text{def}}{=} \gamma p_0$. The experimentally observed quantity is the photoinduced THz transmission change $x(t) \stackrel{\text{def}}{=} (\Delta T/T)(t)$, which is linearly related to the free carrier density (see (1) and (3)):

$$n(t) = \varphi C x(t). \quad (7)$$

Here $C = \tilde{n}_0/x(0)$ is the proportionality factor between the immediate THz response $x(0)$ and the absorbed photon density

$$\tilde{n}_0 = \frac{E\lambda \alpha(\lambda)}{hc A_{\text{eff}}} (1 - R_{\text{pump}}), \quad (8)$$

which can be calculated from the pump beam parameters and the absorption coefficient of the sample α at the excitation wavelength λ .

Substituting (7) into (5) we obtain

$$\begin{aligned} \frac{dx}{dt} &= -C\varphi k_2 x^2 - k_1 x \\ &= -A_2 x^2 - A_1 x \end{aligned} \quad (9)$$

with $A_2 = C\varphi k_2 = C\varphi\gamma$ and $A_1 = k_1 = \gamma p_0$. We fit solutions to this equation simultaneously to all acquired THz transients of a fluence-dependent set (i.e. there is only one globally optimized value for each of the two rate constants A_1 and A_2 , which is applied to all fluences). As the photon-to-free-carrier conversion ratio φ is unknown, we can, strictly speaking, only determine the values $\varphi\gamma = A_2/C$ and $\varphi^{-1}p_0 = CA_1/A_2$ from our fits. These equal the actual decay rate constant γ and hole-doping density p_0 in case the material exhibits full photon-to-free-charge conversion.

To account for the spatially varying charge density profile, our fit routine takes into account the exponential charge density profile created by the pump beam by dividing the sample into 50 equally thick slabs and computing the decay function for all of these individually.

Diffusion length calculation

From the effective mobility and the recombination rate constants extracted from the THz photoconductivity transients we can calculate the charge-carrier diffusion length as follows:

$$L(n) = \sqrt{\frac{D}{R(n)}} = \sqrt{\frac{\mu k_B T}{e R(n)}} \quad (10)$$

with the D being the diffusion coefficient, T the temperature, e the electronic charge, and the R the total carrier recombination rate

$$R(n) = -\frac{1}{n} \frac{dn}{dt} = \varphi \gamma (n/\phi) + \gamma p_0. \quad (11)$$

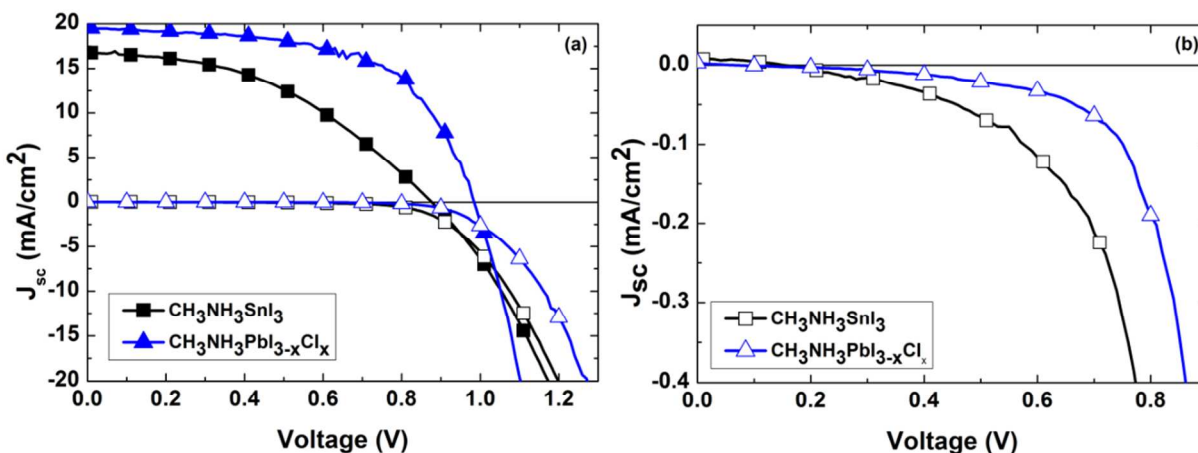


Figure S4: Current-Voltage Characteristics. (a) The current density-voltage (JV) characteristics of the best performing TiO_2 based $\text{CH}_3\text{NH}_3\text{SnI}_3$ (black) and $\text{CH}_3\text{NH}_3\text{PbI}_{3-x}\text{Cl}_x$ (blue) devices. The dark JV curves are represented by the hollow symbols. (b) A zoom in on the current scale for the dark JV curves for both devices, with $\text{CH}_3\text{NH}_3\text{PbI}_{3-x}\text{Cl}_x$ shown in blue and $\text{CH}_3\text{NH}_3\text{SnI}_3$ in black.

Leakage current

The light and dark current voltage characteristics for the best performing Pb-based and Sn-based perovskite devices fabricated on TiO_2 are shown in **Figure S4**. We note here that while the leakage current of the $\text{CH}_3\text{NH}_3\text{SnI}_3$ based device is larger than the leakage current of its Pb counterpart, they are not greatly dissimilar. It is possible that in the best performing devices such as this, the background density of holes due to self-doping is lower than the hole density in other devices which show poorer performance. The uncontrolled nature of this self-doping mechanism can therefore be used to account for the large spread in the V_{oc} of a given batch, as the doping density will presumably vary from device to device. The light JV characteristics of devices with a spread of power conversion efficiencies are presented below in **Figure S5** along with the corresponding dark JV curves.

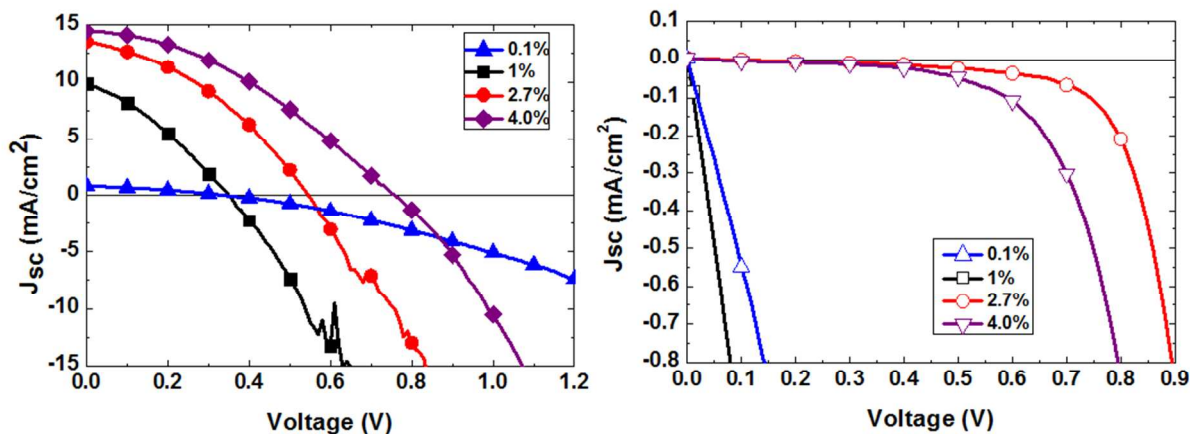


Figure S5: Current-Voltage Characteristics of Various $\text{CH}_3\text{NH}_3\text{SnI}_3$ Devices. (a) Current-voltage (JV) characteristics of $\text{CH}_3\text{NH}_3\text{SnI}_3$ devices of a spread power conversion efficiencies (PCE) under illumination. The PCEs of the devices are as follows: 0.1% (blue triangles), 1% (black squares), 2.7 % (red circles), 4.0% (purple diamonds). (b) Corresponding dark JV characteristics for the devices shown in (a), represented by hollow symbols.

The graphs above show the JV characteristics for devices with a range of power conversion efficiencies from 0.1% to 4%. In the case of the worst performing devices, we propose that the self-doping problem is so severe that it causes short-circuiting of the device. We see from the graphs presented in Figures S4 and S5 that a decrease in the doping density, and thus the leakage current of the device, corresponds to an increase in the performance of the devices. This presents strong motivation for the control of this doping mechanism, as it promises to greatly increase the efficiency of these devices.

References

1. Němec, H.; Kužel, P.; Sundström, V. Far-Infrared Response of Free Charge Carriers Localized in Semiconductor Nanoparticles. *Phys. Rev. B* **2009**, *79*, 115309.

2. Hendry, E.; Koeberg, M.; O'Regan, B.; Bonn, M. Local field effects on electron transport in nanostructured
3. Stoumpos, C. C.; Malliakas, C. D.; Kanatzidis, M. G. Semiconducting Tin and Lead Iodide Perovskites with Organic Cations: Phase Transitions, High Mobilities, and Near-Infrared Photoluminescent Properties. *Inorg. Chem.* **2013**, *52* (15), 9019-9038.
4. Nienhuys, H.-K.; Sundström, V. Intrinsic Complications in the Analysis of Optical-Pump, Terahertz Probe Experiments. *Phys. Rev. B* **2005**, *71*, 235110.
5. Ulbricht, R.; Hendry, E.; Shan, J.; Heinz, T. F.; Bonn, M. Carrier dynamics in semiconductors studied with time-resolved terahertz spectroscopy. *Rev. Mod. Phys.* **2011**, *83*, 543-586.
6. Stranks, S. D.; Eperon, G. E.; Grancini, G.; Menelaou, C.; Alcocer, M. J. P.; Leijtens, T.; Herz, L. M.; Petrozza, A.; Snaith, H. J. Electron-Hole Diffusion Lengths Exceeding 1 Micrometer in an Organometal Trihalide Perovskite Absorber. *Science* **2013**, *342* (6156), 341-344.
7. Xing, G.; Mathews, N.; Sun, S.; Lim, S. S.; Lam, Y. M.; Grätzel, M.; Mhaisalkar, S.; Sum, T. C. Long-Range Balanced Electron- and Hole-Transport Lengths in Organic-Inorganic
8. Wehrenfennig, C.; Liu, M.; Snaith, H. J.; Johnston, M. B.; Herz, L. M. Homogeneous Emission Line Broadening in the Organo Lead Halide Perovskite $\text{CH}_3\text{NH}_3\text{PbI}_{3-x}\text{Cl}_x$. *J. Phys. Chem. Lett.* **2014**, *5*, 1300–1306.